

# Nuclear Magnetic Relaxation Time near the Compensation Temperature in a Ferrimagnetic Insulator

Michiyasu Mori

*Advanced Science Research Center, Japan Atomic Energy Agency, Tokai, Ibaraki 117-1195, Japan*

The nuclear magnetic relaxation time  $T_1$  in a ferrimagnetic insulators is calculated within the mean-field approximation for the magnetic exchange interactions and the Raman process involving the hyperfine interaction. We find that the value of  $1/T_1$  on one type of site increases rapidly near the compensation temperature  $T_0$ , whereas that on the other type of site does not increase up to Curie temperature  $T_c$ . This is due to the fact that the soft-magnon bandwidth becomes comparable to  $T_0$ . An increase in  $1/T_1$  below  $T_c$  is found also in another type ferrimagnet, which shows a hump structure in the temperature dependence of magnetization instead of compensation. Also in that case, we find the rapid increase in  $1/T_1$  below  $T_c$ , even though the magnetization does not show compensation. The coexistence of soft and hard magnons leads to these remarkable properties of ferrimagnets.

## 1. Introduction

A *ferrimagnet* is a kind of *ferromagnet*, and it was theoretically predicted by Néel.<sup>1–3)</sup> Soon afterward, the magnetization compensation was observed in the LiFeCr spinel ferrite, for which the magnetization becomes zero at magnetization-compensation temperature  $T_M$  far below the Curie temperature  $T_c$ .<sup>4)</sup> Such a ferrimagnet, called an N-type ferrimagnet, also has been found in rare-earth iron garnets (RIGs).<sup>2,5–11)</sup> The RIGs have been studied by many authors in order to apply their magnetization-compensation properties to magneto-optical memories.<sup>12–14)</sup>

The dynamical aspects of ferrimagnetism were initially studied using the electron spin resonance (ESR).<sup>15–23)</sup> The ferrimagnetic resonance (FIR) differs from the ferromagnetic resonance (FMR) in having two branches. One gives the usual FMR, while the other, called the exchange frequency, is located higher in energy.<sup>21)</sup> It was difficult to measure the exchange frequency when it was first discovered, since its wavelength is of the order of a tenth of a millimeter. However, a singular behavior of the gyromagnetic ratio was observed around the angular momentum compensation temperature  $T_A$  in a LiFeCr spinel ferrite.<sup>15,16)</sup> On the lower branch, the effective gyromagnetic ratio becomes small around  $T_M$  and then increases rapidly around  $T_A$ .<sup>15–23)</sup> The  $g$ -value of the upper branch becomes small in a measurable range around  $T_A$ .<sup>16)</sup> The magnetization is the product of the Lande  $g$ -factor and a total angular momentum. In general, hence,  $T_M$  is different from  $T_A$ , when the orbital angular momentum is involved. In contrast to the magnetization, the dynamics of a ferrimagnet become singular around  $T_A$ .

Because the magnetization couples to a magnetic field, while the total angular momentum itself does not, it can be difficult to measure  $T_A$  directly using conventional methods. Recently, however, Imai et al. have successfully observed  $T_A$  using the Barnett effect.<sup>24–26)</sup> In a rotating frame, the rotation frequency couples to the angular momentum instead of to the magnetization, without any coupling constant. By spin-rotation coupling, a magnetization is induced through the angular momentum by mechanical rotation. This was originally studied by Barnett,<sup>27)</sup> and it is now used to determine  $T_A$  in

a RIG.<sup>24,25)</sup> It has been reported that around  $T_A$  the magnetization reverse rapidly and that domain walls move fast.<sup>28–31)</sup> Those properties, which are advantageous for magnetic memories, are attributed to angular-momentum compensation.

Nuclear magnetic resonance (NMR) also is a powerful tool for studying the magnetism of a broad range of materials. Magnetic excitations can be characterized by the nuclear magnetic relaxation time  $T_1$ , which originates in the hyperfine interaction between electron and nucleus. For magnetic insulators, however, the origin of  $T_1$  is not so obvious. If the system is isotropic and the nuclear and electron quantization axes are identical, the relaxation cannot be obtained within the linearized spin-wave approximation. Misalignment of the quantization axes—and/or the dipole-dipole interactions between an electronic and a nuclear spins—induces relaxation through the Raman process.<sup>32–34)</sup> Interactions among magnons are also the source of relaxation, e.g., through the three-magnon process.<sup>32–34)</sup> Those processes can be studied for both ferromagnetic and antiferromagnetic insulators. Recently, Imai et al. have reported an enhancement of the NMR signal around  $T_A$ , which is closely related to domain wall motion.<sup>26)</sup> In contrast to ESR, NMR provides a site-selective measurement of magnetism. It is therefore interesting to study the dynamical aspects of magnetism site-by-site in a ferrimagnet. In addition, a consistent understanding of ferrimagnetism among experimental methods—NMR, ESR, and neutron scattering—will be useful.

In this paper, we study the nuclear magnetic relaxation time in ferrimagnets. Section 2 explains the model Hamiltonian and the approximation used. The nuclear magnetic relaxation time due to the Raman process is given in Sec. 3. Additional changes due to orbital angular momentum are briefly discussed in Sec. 4. Below, Bohr magneton  $\mu_B$  and Planck constant  $\hbar = h/2\pi$  are set equal to 1 for brevity.

## 2. Formalism: Magnons in Ferrimagnet

We will focus on a ferrimagnetic “insulator,” which is simply called a “ferrimagnet” below. The magnetic exchange interaction due to the Pauli principle and to the Coulomb interaction between electrons is the source of magnetism in a ferrimagnet. Two sub-lattices with different spin magnitudes

$S_A \neq S_B$  comprise the simplest model. The Hamiltonian is given by

$$H = -J_A \sum_{\langle i,i' \rangle} \vec{S}_i \cdot \vec{S}_{i'} - J_B \sum_{\langle j,j' \rangle} \vec{S}_j \cdot \vec{S}_{j'} + J_C \sum_{\langle i,j \rangle} \vec{S}_i \cdot \vec{S}_j, \quad (1)$$

with the spin operators  $\vec{S}_i$  ( $\vec{S}_j$ ) on site  $i \in A$ -sites ( $j \in B$ -sites). The angular brackets  $\langle \dots \rangle$  denotes nearest neighbor sites. The magnitudes of the magnetic exchange interactions  $J_A$ ,  $J_B$ , and  $J_C$  are assumed to be positive for brevity. First, we do not consider the orbital angular momentum  $\vec{L}_i$ . Hence, there is only one compensation temperature  $T_0$ ; i.e.,  $T_M = T_A \equiv T_0$ . What is changed by  $\vec{L}_i$  will be discussed in the last section. At  $T_0$ , the expectation values  $\langle S_A^z \rangle \equiv M_A > 0$  and  $\langle S_B^z \rangle \equiv -M_B < 0$  satisfy  $M_A - M_B = 0$ , where the bracket denotes the thermal average. See also Appendix A. It is known that there are some possible cases of compensation. In the case considered above, both sub-lattices have the same number of sites in a unit cell, as shown in the inset of Fig. 1. Another case has  $M_A n_A - M_B n_B = 0$ , for which the number  $n_A$  of spins on sub-lattice  $A$  is different from the number  $n_B$  on sub-lattice  $B$ . As shown in Appendix B, those lattice structures have characteristic features in common. Hence, we consider the simplest case, shown in Fig. 1 below.

Compensation occurs at a finite temperature. To include the temperature dependences of  $M_A$  and  $M_B$ , we adopt the mean-field approximation and use the linearized spin-wave approximation around the mean-field solution. This is equivalent to Tyablikov decoupling in the Green's function method and is a kind of random-phase approximation.<sup>35,36</sup> The mean-field solution for  $J_A=0.1$ ,  $J_B=1.0$ ,  $J_C=0.05$ ,  $S_A=1$ , and  $S_B=1/2$ , is shown in Fig. 1, where  $T_0/T_c \sim 0.3$  and the Curie temperature is  $T_c \sim 3.0$ .

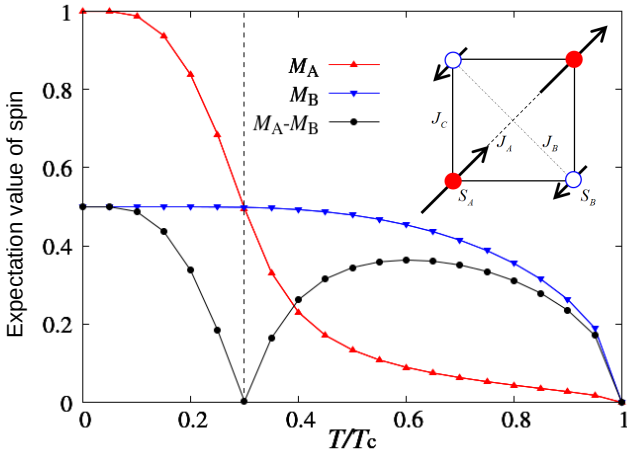


**Fig. 1.** (Color online) The mean-field solution for  $J_A=0.1$ ,  $J_B=1.0$ ,  $J_C=0.05$ ,  $S_A=1$ , and  $S_B=1/2$ . The inset shows the lattice structure, which is three dimensional. The red (upward) and blue (downward) triangles denote  $M_A$  and  $M_B$ , respectively. The black circles are the sum of two expectation values,  $M_A - M_B$ . The broken line indicates  $T_0$ .

The Holstein-Primakoff (HP) bosons (magnons)—for which the creation and annihilation operators are  $a_i^\dagger, a_i$  on  $A$ -sublattice and  $b_j^\dagger, b_j$  on  $B$ -sublattice—are given by,  $S_i^- \sim \sqrt{2M_A} a_i^\dagger$ ,  $S_i^+ \sim \sqrt{2M_A} a_i$ ,  $S_i^z = M_A - a_i^\dagger a_i$ ,  $S_j^- \sim \sqrt{2M_B} b_j^\dagger$ ,  $S_j^+ \sim \sqrt{2M_B} b_j$ ,  $S_j^z = M_B - b_j^\dagger b_j - M_B$ . Below, the spins are assumed to be ordered in the  $z$ -direction. By the linearized approximation, the action of the magnons is given by<sup>37</sup>

$$S = \sum_{q, i\omega_n} \Phi^\dagger \left[ \begin{pmatrix} -i\omega_n & 0 \\ 0 & i\omega_n \end{pmatrix} + \begin{pmatrix} \varepsilon_{1q} & \varepsilon_{3q}^* \\ \varepsilon_{3q} & \varepsilon_{2q} \end{pmatrix} \right] \Phi, \quad (2)$$

$$\Phi^\dagger \equiv (a_q^\dagger(i\omega_n), b_{-q}(-i\omega_n)), \quad (3)$$

$$\varepsilon_{1q} \equiv z J_C M_B + z_A J_A M_A (1 - \zeta_{Aq}), \quad (4)$$

$$\varepsilon_{2q} \equiv z J_C M_A + z_B J_B M_B (1 - \zeta_{Bq}), \quad (5)$$

$$\varepsilon_{3q} \equiv J_C \sqrt{M_A M_B} \sum_{\xi} e^{iq \cdot \xi}, \quad (6)$$

$$\zeta_{A(B)q} \equiv \frac{1}{z_{A(B)}} \sum_{\eta} \cos(\mathbf{q} \cdot \boldsymbol{\eta}), \quad (7)$$

We use the boson operators  $a_q(i\omega_n)$  and  $b_{-q}(-i\omega_n)$  with momentum  $\mathbf{q}=(q_x, q_y, q_z)$  and Matsubara frequency  $\omega_n$ . The  $\mathbf{q}$ -summation is taken over the first Brillouin zone. The magnon dispersion relation depends on the connectivity of the sub-lattice, which gives the number of nearest-neighbor sites  $z_A$  and  $z_B$  on each sub-lattice, and the number  $z$  of nearest-neighbor sites between the two sub-lattices. In Eqs. (6) and (7),  $\xi$  and  $\eta$  mean the summation over the nearest-neighbor sites between the two sub-lattices and within each sublattice, respectively. From Eq. (2), the magnon Green's functions  $g_\nu(\mathbf{q}, i\omega_n)$  are given by

$$\begin{aligned} g_A(\mathbf{q}, i\omega_n) &\equiv \langle a_q(i\omega_n) a_q^\dagger(i\omega_n) \rangle \\ &= -\frac{i\omega_n + \varepsilon_{2q}}{(i\omega_n - E_{\alpha q})(i\omega_n + E_{\beta q})}, \end{aligned} \quad (8)$$

$$\begin{aligned} g_B(\mathbf{q}, i\omega_n) &\equiv \langle b_q(i\omega_n) b_q^\dagger(i\omega_n) \rangle \\ &= -\frac{i\omega_n + \varepsilon_{1q}}{(i\omega_n - E_{\beta q})(i\omega_n + E_{\alpha q})}, \end{aligned} \quad (9)$$

and the magnon dispersion relations  $E_{\alpha q}$  and  $E_{\beta q}$  are given by

$$E_{\alpha q} = \frac{1}{2} \left[ (\varepsilon_{1q} - \varepsilon_{2q}) + \sqrt{(\varepsilon_{1q} + \varepsilon_{2q})^2 - 4|\varepsilon_{3,q}|^2} \right], \quad (10)$$

$$E_{\beta q} = \frac{1}{2} \left[ -(\varepsilon_{1q} - \varepsilon_{2q}) + \sqrt{(\varepsilon_{1q} + \varepsilon_{2q})^2 - 4|\varepsilon_{3,q}|^2} \right]. \quad (11)$$

The small- $Q$  approximation for  $M_A > M_B$  leads to,

$$E_{\alpha q} \sim C Q^2, \quad (12)$$

$$E_{\beta q} \sim 12J_C (M_A - M_B) + D Q^2, \quad (13)$$

where  $C$  and  $D$  are constants given in Appendix B and  $Q \equiv \sqrt{q_x^2 + q_y^2 + q_z^2}$ . The mode  $E_{\alpha q}$  is gapless, while  $E_{\beta q}$  has an "optical gap,"  $E_g \equiv |E_{\alpha q=0} - E_{\beta q=0}| = 12J_C (M_A - M_B)$ , which disappears at  $T_0$ . The dispersion relations degenerate at the gamma point and increases linearly with  $Q$ , similar to an anti-ferromagnet. Away from the gamma point, on the other hand, the two dispersion relations deviate from each other:

$$E_{\alpha q} \sim C_1 Q + C_2 Q^2, \quad (14)$$

$$E_{\beta q} \sim C_1 Q - C_2 Q^2, \quad (15)$$

where  $C_1$  and  $C_2$  are constants given in Appendix B. These  $Q$ -dependences are relevant to the temperature dependence of  $T_1$  at low temperatures.

### 3. Results: Nuclear Magnetic Relaxation due to the Raman Process

In this study, we consider the nuclear magnetic relaxation time  $T_1$  originating from the contact interaction between a nucleus and an electron

$$H_{n-cl} = \frac{1}{2} \sum_{\nu=A,B} \left[ \gamma_\nu \sum_i f_{i\nu} (S_i^z \cdot \vec{I}_i) \right], \quad (16)$$

with the  $g$ -factor on  $\nu$ -sites being given by  $\gamma_\nu$  and the nuclear spin  $\vec{I}_i$  on  $i$ -site. If the system is isotropic and the quantization axes of the nucleus and electron are identical, we cannot obtain relaxation within the linearized approximation. Misalignment of the quantization axes—and/or the dipole-dipole interactions between electronic and nuclear spins—will induce relaxation due to the Raman process.<sup>32–34</sup> Interactions among magnons also cause relaxation, e.g., through the three magnon-process.<sup>32–34</sup> Below, we focus on the Raman process induced by misalignment. This is sufficient to enable us to find some of the characteristics of  $T_1$  near  $T_0$ . The critical exponent of  $T_1$  is beyond the scope of this study and will be discussed elsewhere. When the quantization axis of nucleus deviates by an angle  $\theta$  from that of the electron, Eq. (16) reduces to the following component

$$H_{n-cl}^z = \frac{1}{2} \sum_{\nu=A,B} \left[ \gamma_\nu \sum_i \sin \theta f_{i\nu} S_i^z (I_i^+ + I_i^-) \right], \quad (17)$$

which are relevant for calculating  $T_1$ . Assuming that  $\gamma_A = \gamma_B \equiv \gamma$  and the form factors  $f_{iA}$  are constant, i.e.,  $f_{iA} = f_{iB} \equiv f$ , the  $T_1$  on site  $\nu = A, B$  is given by

$$\frac{1}{T_{1\nu}} = F \sum_{\mathbf{q}} C_\nu(\mathbf{q}, \omega_0), \quad (18)$$

$$C_\nu(\mathbf{q}, \omega_0) = \int dt e^{i\omega_0 t} \langle S_{\nu\mathbf{q}}^z(t) S_{\nu-\mathbf{q}}^z(0) + S_{\nu-\mathbf{q}}^z(t) S_{\nu\mathbf{q}}^z(0) \rangle, \quad (19)$$

where  $\langle \dots \rangle$  means the thermal average. The nuclear magnetic resonance energy is denoted by  $\omega_0$ , and  $F = (\gamma f \sin \theta / 2)^2$ . Using Eqs. (8) and (9), the spin-spin correlation function  $C_\nu(\mathbf{q}, \omega_0)$  is given by

$$C_\nu(\mathbf{q}, \omega_0) = \frac{2}{1 - e^{\omega_0/k_B T}} \text{Im} \Pi_\nu^R(\mathbf{q}, \omega_0), \quad (20)$$

$$\Pi_\nu(\mathbf{q}, i\omega_0) = k_B T \sum_{\mathbf{p}, n} g_\nu(\mathbf{p} + \mathbf{q}, i\omega_n + i\omega_0) g_\nu(\mathbf{p}, i\omega_n), \quad (21)$$

where  $T$  is temperature,  $k_B$  is the Boltzmann's constant, and momentum  $\mathbf{p} = (p_x, p_y, p_z)$  in the first Brillouin zone. The retarded function of  $\Pi_\nu(\mathbf{q}, i\omega_0)$  is denoted by  $\Pi_\nu^R(\mathbf{q}, \omega_0)$ . When  $\omega_0$  is much smaller than  $k_B T$ , the nuclear magnetic relaxation time  $T_{1\nu}$  on site  $\nu$  is given by

$$\frac{1}{T_{1\nu}} = 2F \sum_{\mathbf{q}} \lim_{\omega_0 \rightarrow 0} \frac{k_B T}{\omega_0} \text{Im} \Pi_\nu^R(\mathbf{q}, \omega_0), \quad (22)$$

$$= 2\pi F \sum_{\mathbf{p}, \mathbf{q}} \left\{ n_B(E_{\nu\mathbf{p}}) [n_B(E_{\nu\mathbf{p}}) + 1] \frac{\alpha_{\mathbf{p}} \alpha_{\mathbf{q}}}{\Delta_{\mathbf{p}} \Delta_{\mathbf{q}}} \delta(E_{\nu\mathbf{p}} - E_{\nu\mathbf{q}}) \right.$$

$$\left. + n_B(E_{\mu\mathbf{p}}) [n_B(E_{\mu\mathbf{p}}) + 1] \frac{\beta_{\mathbf{p}} \beta_{\mathbf{q}}}{\Delta_{\mathbf{p}} \Delta_{\mathbf{q}}} \delta(E_{\mu\mathbf{p}} - E_{\mu\mathbf{q}}) \right\}, \quad (23)$$

$$\frac{\alpha_{\mathbf{p}}}{\Delta_{\mathbf{p}}} = \frac{1}{2} \left( \frac{\varepsilon_{1\mathbf{p}} + \varepsilon_{2\mathbf{p}}}{\Delta_{\mathbf{p}}} + 1 \right), \quad (24)$$

$$\frac{\beta_{\mathbf{p}}}{\Delta_{\mathbf{p}}} = \frac{1}{2} \left( \frac{\varepsilon_{1\mathbf{p}} + \varepsilon_{2\mathbf{p}}}{\Delta_{\mathbf{p}}} - 1 \right), \quad (25)$$

$$\Delta_{\mathbf{p}} = \sqrt{(\varepsilon_{1\mathbf{p}} + \varepsilon_{2\mathbf{p}})^2 - 4|\varepsilon_{3\mathbf{p}}|^2}, \quad (26)$$

Here  $\mu \neq \nu$ , i.e.,  $\mu=\alpha$  for  $\nu=\beta$  or  $\mu=\beta$  for  $\nu=\alpha$  and the Bose distribution function is denoted by  $n_B(x) \equiv 1/[e^{x/(k_B T)} - 1]$ . Note that Eq. (23) can be checked by considering the ferro- and the antiferromagnet cases as discussed in Appendix C.

Using Eq. (23) and the mean-field solution shown in Fig. 1, the  $T$ -dependence of  $1/T_{1\nu}$  can be calculated numerically as shown in Fig. 2 (a). Note that  $1/T_{1A}$  increases rapidly around

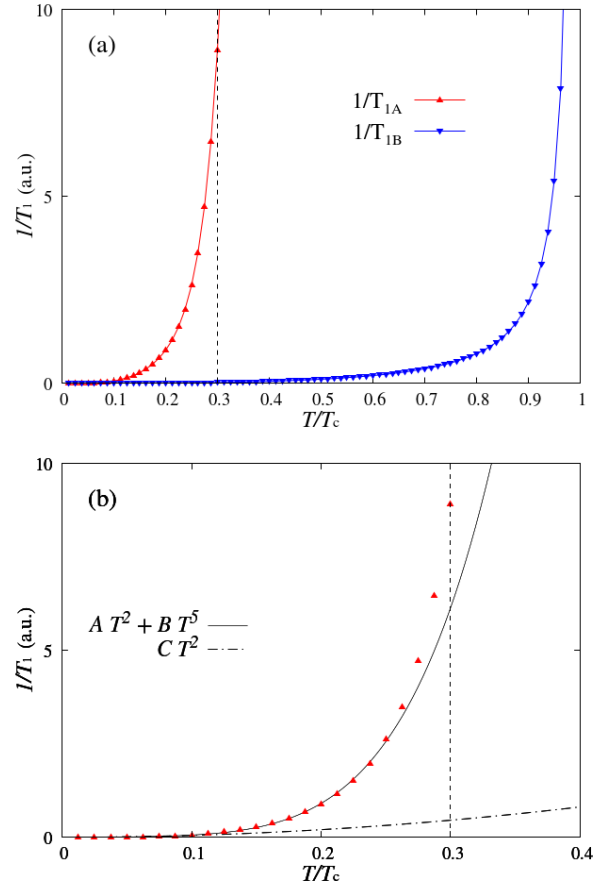


**Fig. 2.** (Color online) (a) The  $T$ -dependence of  $1/T_1$  on the A-sites and B-sites ( $1/T_{1A}$  and  $1/T_{1B}$ ) are plotted with upward triangles (red) and downward triangles (blue), respectively. The mean-field solution for  $J_A=0.1$ ,  $J_B=1.0$ ,  $J_C=0.05$ ,  $S_A=1$ , and  $S_B=1/2$  was used. The broken line indicates  $T_0$ . See also Fig. 1. (b) At low temperatures,  $T_{1A}$  is well fitted by  $T^2$  (the dashed-dotted line) similar to the ferromagnet (See also Appendix C), whereas it is deviated with increasing temperature as  $AT^2 + BT^5$  (solid line).  $A$  and  $B$  are constants.

$T/T_c \sim 0.3$ , which corresponds to  $T_0$  indicated by the broken line in Fig. 2. This contrasts sharply with  $1/T_{1B}$ , which diverges just below  $T_c$ . As shown in Fig. 2 (b), at low temperatures,  $T_{1A}$  is well fitted by  $T^2$ , similar to the ferromagnet

(See also Appendix C). With increasing temperature, on the other hand, it is fitted by  $AT^2 + BT^5$  with constants  $A$  and  $B$ . This is similar to the behavior of a ferromagnet, except for the fact that  $1/T_{1A}$  increases around  $T_0$  instead of  $T_c$ .

To understand this behavior of  $1/T_1$  around  $T_0$ ,  $E_{\alpha q}$  and  $E_{\beta q}$  are plotted in Fig. 3 for (a)  $T/T_c = 0.1$  and (b)  $T/T_c = 0.3$  with  $q_y = q_z = 0$ . At low temperatures, the  $T$ -dependence of  $1/T_1$

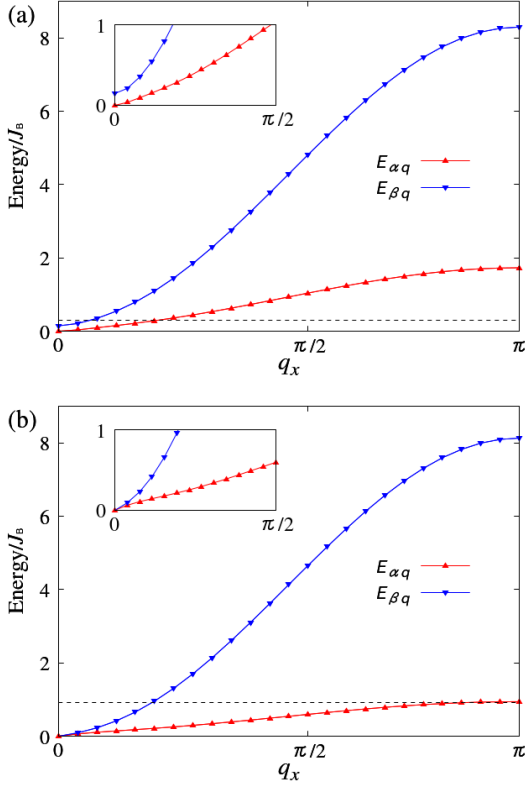


**Fig. 3.** (Color online) The dispersion relations  $E_{\alpha q}$  and  $E_{\beta q}$  are plotted by upward triangles (red) and downward triangles (blue), respectively, for (a)  $T/T_c = 0.1$  and (b)  $T/T_c = 0.3$ , with  $q_y = q_z = 0$ . In the pre-set lattice structure, at  $\mathbf{q} = (\pi, \pi/2, 0)$ ,  $E_{\alpha q}$  is a maximum. This can be approximated by its value at  $\mathbf{q} = (\pi, 0, 0)$  due to the small value of  $J_C$ . The low-energy region is enlarged and plotted in the insets.

is determined by the  $Q^2$ -dependences of  $E_{\alpha q}$  and  $E_{\beta q}$  around  $Q \sim 0$ . See also the inset of Fig. 3 (a). At  $T = T_0$ ,  $E_g$  becomes zero, as shown in the inset of Fig. 3 (b), and both  $E_{\alpha q}$  and  $E_{\beta q}$  become proportional to  $Q$  instead of  $Q^2$  around  $Q = 0$ . Note that  $k_B T/J_B$  is shown by the broken line in Figs. 3 (a) and (b) as a measure of the temperature. In the pre-set lattice structure,  $E_{\alpha q}$  is a maximum at  $\mathbf{q} = (\pi, \pi/2, 0)$ . It can be approximated by the value at  $\mathbf{q} = (\pi, 0, 0)$ , since the small value of  $J_C = 0.05$ . We then find that at  $T = T_0$  the bandwidth of  $E_{\alpha q}$  becomes comparable to  $k_B T$ . This means that all states of  $E_{\alpha q}$  contribute to  $1/T_1$  through  $n_B(x)$  in the first term in Eq. (23), where the first term is dominant. This is the origin of the rapid increase in  $1/T_{1A}$  at  $T_0$ . This is not accidental, due to the following points. The bandwidth of  $E_{\alpha q}$  can be very roughly estimated by  $\varepsilon_{1, \mathbf{q}=(\pi, 0, 0)} \sim (6J_C + 16J_A)M_0 \sim 8J_A = 0.8$  with  $M_A = M_B \equiv M_0 \sim 0.5$ . On the other hand,  $T_0$  can be roughly estimated as  $T_0 \sim z_A J_A X_A = 0.8$ . Since  $M_A$  is soft and decreases rapidly with  $T$ ,  $T_0$  is close to the Curie temperature of a system limited to the  $A$ -sublattice. Therefore,  $1/T_{1A}$

rapidly increases around  $T_0$ .

So far, we have discussed an  $N$ -type ferrimagnet.<sup>1,3)</sup> Another type of ferrimagnet—called  $P$ -type—shows a hump in the temperature dependence of the magnetization instead of compensation. Figure 4 is calculated from Eq. (1) for  $J_A=0.5$ ,  $J_B=1.0$ ,  $J_C=0.2$ ,  $S_A=1/2$ , and  $S_B=1$ . The lattice structure is the same as the inset of Fig. 1. In a  $P$ -type ferrimagnet, the

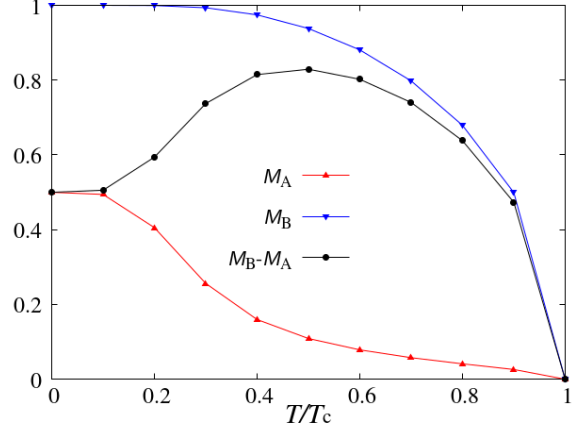


**Fig. 4.** (Color online) The mean-field solution for a  $P$ -type ferrimagnet with  $J_A=0.5$ ,  $J_B=1.0$ ,  $J_C=0.2$ ,  $S_A=1/2$ , and  $S_B=1$ .

magnetization does not show any singular behavior, such as compensation, although it is composed of two different sublattices, i.e., with soft and hard dispersion relations  $E_{\alpha q}$  and  $E_{\beta q}$ . The value of  $1/T_{1v}$  in a  $P$ -type ferrimagnet is plotted in Fig. 5 in the same way as for the  $N$ -type. We find that  $1/T_{1A}$

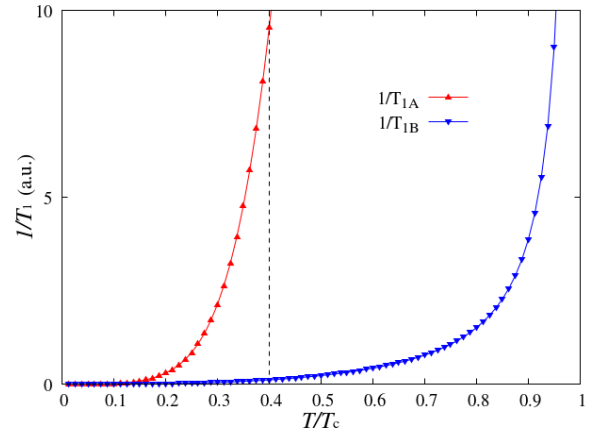


**Fig. 5.** (Color online) The relaxation rate  $1/T_1$  in a  $P$ -type ferrimagnet. The  $T$ -dependences of  $1/T_1$  on the  $A$ -sites and  $B$ -sites ( $1/T_{1A}$  and  $1/T_{1B}$ ) are plotted by upward triangles (red) and downward triangles (blue), respectively. The mean-field solution for  $J_A=0.5$ ,  $J_B=1.0$ ,  $J_C=0.2$ ,  $S_A=1/2$ , and  $S_B=1$  was used. The broken line is near the top of the hump structure.

rapidly increases around  $T/T_c \sim 0.4$  close to the top of the hump structure, while  $1/T_{1B}$  increases rapidly near  $T_c$ . It is now straightforward to understand this behavior, since the  $A$ -sublattice is soft and the  $B$ -sublattice is hard. This is clearly shown by the dispersion relation in Figs. 6 for (a)  $T/T_c = 0.1$

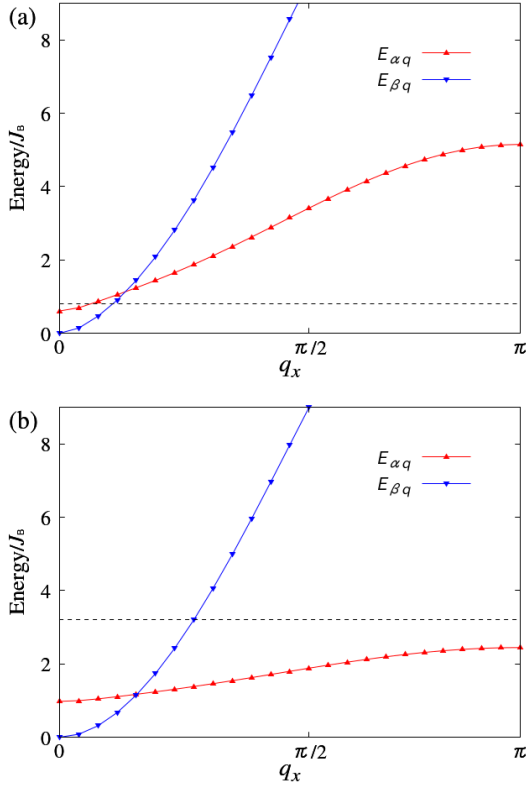


**Fig. 6.** (Color online) The dispersion relations  $E_{\alpha q}$  and  $E_{\beta q}$  are plotted by upward triangles (red) and downward triangles (blue), respectively, for (a)  $T/T_c = 0.1$  and (b)  $T/T_c = 0.4$ , with  $q_y = q_z = 0$ . The broken line indicates the corresponding temperature  $k_B T/J_B$ .

and (b)  $T/T_c = 0.4$ . In each panel,  $k_B T/J_B$  is shown by the broken line as measure of the temperature. At  $T/T_c = 0.4$ , all of  $E_{\alpha q}$  contribute to  $1/T_{1A}$ . Therefore, even in a  $P$ -type ferrimagnet without compensation, we find a rapid increase of  $1/T_1$ .

#### 4. Summary and Discussions

We have studied  $T_1$  in a ferrimagnetic insulator that is induced by the Raman process involving the hyperfine interaction. To calculate  $1/T_1$ , we adopted a Heisenberg model composed of two sublattices and used the linearized spin-wave approximation around the mean-field solution. At  $T_0 < T_c$ ,  $1/T_1$  increases rapidly on one sublattice, whereas on the other site it does not increase up to  $T_c$ , as usual in a ferromagnet. This is due to the fact that an  $N$ -type ferrimagnet has two magnon excitations. The soft magnon contributes to the increasing behavior of  $1/T_1$  at  $T_0$ , since the bandwidth of the soft magnon is less than  $T_0$  in energy.

At low temperatures, the  $T$ -dependence of  $1/T_1$  is well fitted by  $T^2$ , similar to the ferromagnetic case. With increasing temperature, a  $T^5$ -component is added, due to the momentum dependence of the dispersion relation. In this paper, however, we have considered only the Raman process. When the three-magnon process, magnon-magnon interactions, and other factors are involved, those  $T$ -dependences will be modified. Those are beyond the purpose of this paper and will be studied elsewhere.

The increase in  $1/T_1$  below  $T_c$  is found also in a  $P$ -type ferrimagnet, which shows hump structure in the temperature de-

pendence of the magnetization instead of compensation. Also in a  $P$ -type ferrimagnet, we find a rapid increase of  $1/T_1$  below  $T_c$ , even though the magnetization does not show compensation. This also can be explained by the fact that a  $P$ -type ferrimagnet is composed of soft and hard magnons. Although a  $P$ -type ferrimagnet does not show compensation,  $1/T_1$  on one sublattice still increases below  $T_c$ . We expect this to be experimentally confirmed in the near future.

So far, we have not considered the orbital angular momentum  $\vec{L}$ . For example, in rare-earth (R) iron garnets,  $R_3\text{Fe}_5\text{O}_{12}$  ( $R=\text{Ho, Er, Tb, etc.}$ ), the rare-earth magnetization is calculated by using the total angular momentum  $\vec{J} = \vec{L} + \vec{S}$ .<sup>38)</sup> The Landé  $g$ -factor on an R-site is different from that on an iron site, and  $T_M \neq T_A$  in general. Still, Eq. (1) is our starting point. The expectation value of  $S_A^z$  then contains the extra factor  $(\gamma_A - 1)$ , so that  $\langle S_A^z \rangle = (\gamma_A - 1) \langle J_A^z \rangle$ ,<sup>38)</sup> where  $J_v^z$  is the  $z$ -component of  $\vec{J}$  on  $v$ -site ( $v=A, B$ ). These factors can be renormalized into  $J_A, J_B$ , and  $J_C$ :  $K_A \equiv (\gamma_A - 1)^2 J_A$ ,  $K_B \equiv (\gamma_B - 1)^2 J_B$ , and  $K_C \equiv (\gamma_A - 1)(\gamma_B - 1) J_C$ .<sup>39,40)</sup> Using  $K_A, K_B$ , and  $K_C$ , the magnon dispersion relations are obtained by substituting  $\langle J_A^z \rangle$  and  $\langle J_B^z \rangle$  for  $M_A$  and  $M_B$ , respectively. See also Appendix D. Around which temperature,  $T_M$  or  $T_A$ , does  $1/T_1$  start to increase? The magnon bandwidth is determined by the expectation value of  $\langle S_A^z \rangle = (\gamma_A - 1) \langle J_A^z \rangle$  and  $\langle S_B^z \rangle = (\gamma_B - 1) \langle J_B^z \rangle$  instead of  $\langle J_A^z \rangle$  and  $\langle J_B^z \rangle$ . We recall that  $1/T_1$  increases, when  $k_B T$  is comparable to the bandwidth, and  $T_A$  is determined by  $\langle J_A^z \rangle$  and  $\langle J_B^z \rangle$ . For example, in a case with  $\gamma_A=5/4, \gamma_B=2$ , such as for  $\text{Ho}_3\text{Fe}_5\text{O}_{12}$ , the factors  $(\gamma_A - 1)$  and  $(\gamma_B - 1)$  are smaller than 1. A rough estimate of the energy scale of the bandwidth is thus smaller than  $T_A$ . This means that  $1/T_1$  will start to increase further below  $T_A$ . However, those energy scales are different depending on the materials involved. Thus, it is difficult to identify the temperature at which  $1/T_1$  starts to increase. Such a material dependence will be discussed in the near future and will be clarified experimentally.

On the other hand, it is clear that  $E_g$  becomes zero at  $T_A$  instead of  $T_M$

$$E_g = 12K_C \left[ \langle J_A^z \rangle - \langle J_B^z \rangle \right]. \quad (27)$$

Magnon excitations in RIGs have been reported from inelastic neutron scattering.<sup>41,42)</sup> However,  $E_g$  has not yet been clarified around the compensation temperature. The loss of  $E_g$  must be associated with the increase of domain wall speed at  $T_A$ <sup>28-31)</sup> and the enhancement of NMR signals.<sup>26)</sup> Such remarkable changes of the domain walls will make ferrimagnets more useful for spintronics. A consistent understanding of the NMR, ESR, and neutron-scattering results will be even more important and useful.

The author thanks S. Maekawa, H. Chudo, M. Imai, M. Fujita, Y. Kawamoto, S. Kambe, Y. Tokunaga, and H. Sakai for useful and helpful discussions. This work was supported by Grants-in-Aid for Scientific Research (Grant 18H04492 and 20K03810) from JSPS and MEXT, and by the inter-university cooperative research program of IMR Tohoku University (20N0006). A part of the numerical calculation was done with the supercomputer of JAEA.

## Appendix A: Mean-field Equation

The mean-field equation and its solution are straightforward. We define

$$M_A = f_{S_A} [(z_A J_A M_A - z_J J_C M_B) / (k_B T)], \quad (\text{A}\cdot 1)$$

$$M_B = f_{S_B} [(z_B J_B M_B - z_J J_C M_A) / (k_B T)], \quad (\text{A}\cdot 2)$$

$$f_S [x] \equiv (S + 1/2) \coth [x(S + 1/2)] - 1/2 \coth (x/2). \quad (\text{A}\cdot 3)$$

Note that  $g$  and  $\mu_B$  have been omitted to make the equations clearer. Solving Eqs. (A·1) and (A·2) gives  $T_C$  in the form

$$T_C = \frac{1}{2} \left[ X_A z_A J_A + X_B z_B J_B + \sqrt{(X_A z_A J_A - X_B z_B J_B)^2 + X_A X_B (2z_J J_C)^2} \right], \quad (\text{A}\cdot 4)$$

$$X_A \equiv (S_A + 1)S_A/3, \quad (\text{A}\cdot 5)$$

$$X_B \equiv (S_B + 1)S_B/3, \quad (\text{A}\cdot 6)$$

For the case shown in Fig. 1,  $T_0$  can be approximated by the Curie temperature of the system limited to the  $A$ -sublattice, it is given by  $T_0 \sim z_A J_A X_A$ .

## Appendix B: Magnon Dispersion Relations in a Ferromagnet

At low energies away from the compensation temperature, the magnon dispersion relations given by Eqs. (10) and (11) can be expanded as

$$E_{\alpha q} \sim C Q^2, \quad (\text{B}\cdot 1)$$

$$E_{\beta q} \sim 12J_C (M_A - M_B) + D Q^2, \quad (\text{B}\cdot 2)$$

$$C = \frac{[3J_A M_A^2 - (J_A + J_B - 2J_C) M_A M_B + 3J_B M_B^2]}{M_A - M_B}, \quad (\text{B}\cdot 3)$$

$$D = \frac{J_A M_A^2 - (3J_A + 3J_B + 2J_C) M_A M_B + J_B M_B^2}{M_A - M_B}, \quad (\text{B}\cdot 4)$$

$$\varepsilon_{1q} + \varepsilon_{2q} = 6J_C (M_A + M_B) + 4(J_A M_A + J_B M_B) Q^2, \quad (\text{B}\cdot 5)$$

$$\Delta_q = 6J_C (M_A - M_B) + \frac{12J_C (M_B + M_A) (J_A M_A + J_B M_B) + 24J_C^2 M_A M_B}{6J_C (M_A - M_B)} Q^2, \quad (\text{B}\cdot 6)$$

where  $Q \equiv \sqrt{q_x^2 + q_y^2 + q_z^2}$ . Note that  $(0,0,0)$  and  $(\pi, \pi, \pi)$  are equivalent for the case shown in Fig. 1. At the compensation temperature  $M_A = M_B \equiv M$ , the excitation gap vanishes

$$E_{\alpha q} \sim C_2 Q^2 + C_1 Q, \quad (\text{B}\cdot 7)$$

$$E_{\beta q} \sim -C_2 Q^2 + C_1 Q, \quad (\text{B}\cdot 8)$$

$$C_1 = 2\sqrt{3}J_C (J_A + J_B + J_C) S, \quad (\text{B}\cdot 9)$$

$$C_2 = 2(J_A - J_B) S, \quad (\text{B}\cdot 10)$$

$$\varepsilon_{1q} + \varepsilon_{2q} = 12J_C S + 4(J_A + J_B) S Q^2, \quad (\text{B}\cdot 11)$$

$$\Delta_q = 4S \sqrt{3J_C (J_A + J_B + J_C)} Q. \quad (\text{B}\cdot 12)$$

This does not depend on the lattice structure, as shown in Fig. B·1.

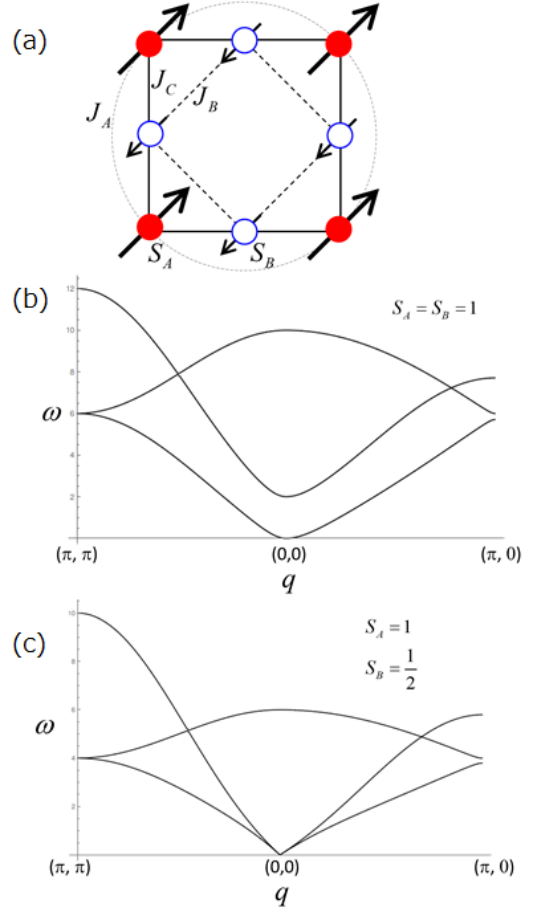


**Fig. B·1.** (Color online) (a) Schematic illustration of the compensation. The  $A$ -sublattice has one site, whereas the  $B$ -sublattice two sites. (b) Magnon dispersion relation away from the compensation point for  $J_A=J_B=J_C=1$ ,  $S_A=S_B=1$ . (c) Magnon dispersion relation at the compensation point for  $J_A=J_B=J_C=1$ ,  $S_A=1$  and  $S_B=1/2$ . In both (b) and (c), the parameters were chosen by hand to show the characteristics.

## Appendix C: Nuclear Magnetic Relaxation in a Ferromagnet and an Antiferromagnet

The ferromagnetic state is obtained by imposing the conditions  $S_B=0$  and  $J_C=J_B=0$  on the mean-field equation given by Eq. (1). Equation (23) then reduces to

$$\frac{1}{T_1} = 2\pi F \sum_{p,q} n_B(E_p) [n_B(E_p) + 1] \times \delta(E_p - E_q), \quad (\text{C}\cdot 1)$$

with  $E_q = z_A J_A M_A (1 - \zeta_{Aq})$ . The temperature dependence of  $1/T_1$  is shown in Fig. C·1. At low temperatures, it is well fitted by  $CT^2$ , because  $E_q \propto Q^2$ .<sup>33,34)</sup> On the other hand, it deviates from  $T^2$  with increasing  $T$  and is well fitted by  $AT^2 + BT^5$ , since a  $Q$ -linear component grows in  $E_q$ . Here,  $A$ ,  $B$ , and  $C$  are constants.

The antiferromagnetic state is given by  $S_A = S_B$  and  $J_A = J_B = 0$ . In this case,  $E_{\alpha q} = E_{\beta q}$ . Equation (23) then reduces to

$$\frac{1}{T_{1,\nu}} = 2\pi A_\nu \sum_{p,q} n_B(E_{\nu p}) [n_B(E_{\nu p}) + 1] \left[ \frac{\varepsilon_p \varepsilon_q}{\Delta_p \Delta_q} + \frac{1}{4} \right]$$

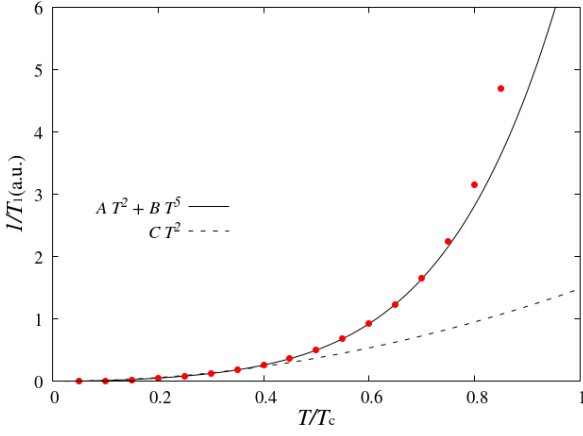


**Fig. C-1.** (Color online) The  $T$ -dependence of  $1/T_1$  in the ferromagnetic state. The red dots were calculated numerically from Eq. (C-1) and the mean-field solution. The thick and the broken lines are fitting results using  $AT^2 + BT^5$  and  $CT^2$ , respectively.

$$\times \delta(E_{vp} - E_{vq}), \quad (\text{C-2})$$

where  $\Delta_p = 2\sqrt{\varepsilon_p^2 - |\varepsilon_{3,p}|^2}$  and  $\varepsilon_p = \varepsilon_{1p} = \varepsilon_{2p}$ . Its temperature dependence is shown in Fig. C-2. At low temperatures, it is

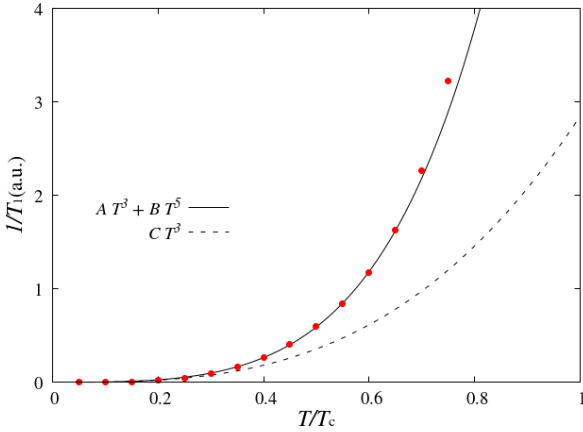


**Fig. C-2.** (Color online) The  $T$ -dependence of  $1/T_1$  in the antiferromagnetic state. The red dots were calculated numerically from Eq. (C-2) and the mean-field solution. The thick and the broken lines are fitting results using  $AT^3 + BT^5$  and  $CT^3$ , respectively.

well fitted by  $CT^3$ , because  $E_q \propto Q$  and  $(\varepsilon_q/\Delta_q) \propto Q^{-1}$ .<sup>32,34</sup> On the other hand, it deviates from  $T^3$  with increasing  $T$  and is well fitted by  $AT^3 + BT^5$ , since the curvature of  $E_q$  becomes relevant. Here,  $A$ ,  $B$ , and  $C$  are constants.

#### Appendix D: ESR Frequencies

When we consider  $\vec{L}$ ,  $J_A$ ,  $J_B$ , and  $J_C$  are replaced by  $K_A$ ,  $K_B$ , and  $K_C$ , and further  $M_A$  and  $-M_B$  are interpreted as  $\langle J_A^z \rangle$  and  $-\langle J_B^z \rangle$  in Eqs. (10) and (11). In a magnetic field  $\vec{H} = (0, 0, H)$ ,  $\gamma_A H$  and  $-\gamma_B H$  are added to Eqs. (4) and (5), respectively. The magnon excitations at  $Q = 0$ , which correspond to the

ESR frequencies  $\Omega_\alpha$  and  $\Omega_\beta$  are given by

$$\Omega_\alpha = \frac{1}{2} \left[ (\varepsilon_1 - \varepsilon_2) + \sqrt{(\varepsilon_1 + \varepsilon_2)^2 - 4|\varepsilon_3|^2} \right], \quad (\text{D-1})$$

$$\Omega_\beta = \frac{1}{2} \left[ -(\varepsilon_1 - \varepsilon_2) + \sqrt{(\varepsilon_1 + \varepsilon_2)^2 - 4|\varepsilon_3|^2} \right]. \quad (\text{D-2})$$

$$\varepsilon_1 = \lambda \langle J_B^z \rangle + \gamma_A H, \quad (\text{D-3})$$

$$\varepsilon_2 = \lambda \langle J_A^z \rangle - \gamma_B H, \quad (\text{D-4})$$

$$\varepsilon_3 = \lambda \sqrt{\langle J_A^z \rangle \langle J_B^z \rangle}, \quad (\text{D-5})$$

with  $\lambda = zK_C$ . At low temperatures—below both  $T_M$  and  $T_A$ —and to first order in  $H$ , Eqs. (D-1) and (D-2) for  $\langle J_A^z \rangle - \langle J_B^z \rangle > 0$  can be approximated as<sup>17-23</sup>

$$\Omega_\alpha \sim \frac{\gamma_A \langle J_A^z \rangle - \gamma_B \langle J_B^z \rangle}{\langle J_A^z \rangle - \langle J_B^z \rangle} H \equiv \gamma_{\text{eff}} H, \quad (\text{D-6})$$

$$\Omega_\beta \sim \lambda (\langle J_A^z \rangle - \langle J_B^z \rangle) - \frac{\gamma_B \langle J_A^z \rangle - \gamma_A \langle J_B^z \rangle}{\langle J_A^z \rangle - \langle J_B^z \rangle} H, \quad (\text{D-7})$$

with the effective gyromagnetic ratio  $\gamma_{\text{eff}}$ . At  $T_A$ , note that the two frequencies become close each other, since  $\Omega_\alpha - \Omega_\beta = (\gamma_A + \gamma_B)H$ .

- 1) L. Néel, Ann. Phys. (Paris) **12** 137 (1948).
- 2) L. Néel, R. Pauthenet, and B. Dreyfus, in *Progress Low Temperature Physics* ed. C.J. Gorter (North Holland, Amsterdam 1964) vol. 4 Chap. VII, p.344.
- 3) L. Néel, Science **174**, 985 (1971).
- 4) E. W. Gorter and J. A. Schulkes, Phys. Rev. **90**, 487 (1953).
- 5) R. Pauthenet and P. Blum, Compt. Rend. **239**, 33 (1954).
- 6) F. Bertaut and F. Forrat Compt. Rend. **242**, 382 (1956).
- 7) S. Geller and M. A. Gilleo, Acta Cryst. **10**, 239 (1957).
- 8) S. Geller and M. A. Gilleo, J. Phys. Chem. Solids **3**, 30 (1957).
- 9) R. Pauthenet, Ann. Phys. **13**, 424 (1958).
- 10) S. Geller, H. J. Williams, R. C. Sherwood, J. P. Remeika, and G. P. Espinosa, Phys. Rev. **131**, 1080 (1963).
- 11) S. Geller, J. P. Remeika, R. C. Sherwood, H. J. Williams, and G. P. Espinosa, Phys. Rev. **137**, A1034 (1965).
- 12) J. T. Chang, J. F. Dillon, and U. F. Gianola, J. Appl. Phys. **36**, 1110 (1965).
- 13) K. Chow, W. Leonard, and R. Comstock, IEEE Trans. Mag. **4**, 416 (1968).
- 14) T. Nelson, IEEE Trans. Mag. **4**, 421 (1968).
- 15) J. S. van Wieringen, Phys. Rev. **90**, 488 (1953).
- 16) T. R. McGuire, Phys. Rev. **97**, 831 (1955).
- 17) J. Kaplan and C. Kittel, J. Chem. Phys. **21**, 760 (1953).
- 18) R. K. Wangsness, Phys. Rev. **91**, 1085 (1953).
- 19) R. K. Wangsness, Phys. Rev. **93**, 68 (1954).
- 20) N. Tsuya, Prog Theor Phys **12**, 1 (1954).
- 21) R. K. Wangsness, Phys. Rev. **97**, 831 (1955).
- 22) S. Geschwind and L. R. Walker, J. Appl. Phys. **30**, S163 (1959).
- 23) J. H. Van Vleck, Phys. Rev. **123**, 58 (1961).
- 24) M. Imai, Y. Ogata, H. Chudo, M. Ono, K. Harii, M. Matsuo, Y. Ohnuma, S. Maekawa, and E. Saitoh, Appl. Phys. Lett. **113**, 052402 (2018).
- 25) M. Imai, H. Chudo, M. Ono, K. Harii, M. Matsuo, Y. Ohnuma, S. Maekawa, and E. Saitoh, Appl. Phys. Lett. **114**, 162402 (2019).
- 26) M. Imai, H. Chudo, M. Matsuo, S. Maekawa, and E. Saitoh, Phys. Rev. B **102**, 014407 (2020).
- 27) S. J. Barnett, Phys. Rev. **6**, 239 (1915).
- 28) X. Jiang, L. Gao, J. Z. Sun, and S. S. P. Parkin, Phys. Rev. Lett. **97**, 217202 (2006).
- 29) C. D. Stanciu, A. Tsukamoto, A. V. Kimel, F. Hansteen, A. Kirilyuk, A. Itoh, and Th. Rasing, Physical Review Letters **99**, 217204 (2007).
- 30) K.-J. Kim, S. K. Kim, Y. Hirata, S.-H. Oh, T. Tono, D.-H. Kim, T. Okuno, W. S. Ham, S. Kim, G. Go, Y. Tserkovnyak, A. Tsukamoto, T. Moriyama,

- K.-J. Lee, and T. Ono, *Nat. Mater.* **16**, 1187 (2017).
- 31) S. K. Kim, K. Nakata, D. Loss, and Y. Tserkovnyak, *Phys. Rev. Lett.* **122**, 057204 (2019).
- 32) T. Moriya, *Prog. Theor. Phys.* **16**, 23 (1956).
- 33) A. H. Mitchell, *J. Chem. Phys.* **27** 17 (1957).
- 34) D. Beeman and P. Pincus, *Phys. Rev.* **166**, 359 (1968).
- 35) S. V. Tyablikov, *Ukrain. Math. Zh.* **11**, 287 (1959).
- 36) T. Oguchi and A. Honma, *J. Appl. Phys.*, **34**, 1153 (1963).
- 37) M. Mori, *J. Phys. Soc. Jpn.* **86**, 124705 (2017).
- 38) J. H. van Vleck, in *The Theory of Electric and Magnetic Susceptibilities* (Oxford University Press, New York, 1932).
- 39) P. G. de Gennes, *Comptes Rendus* **247**, 1836 (1958).
- 40) A. Szutufa, and J. Leciejewicz, in *Handbook on the Physics and Chemistry of Rare Earths* vol. 12, eds. K. A. Gschneider, Jr. and L. Eyring (Elsevier, Amsterdam, 1989) p. 131.
- 41) J. S. Plant, *Journal of Physics C: Solid State Physics* **10**, 4805 (1977).
- 42) Y. Nambu, J. Barker, Y. Okino, T. Kikkawa, Y. Shiomi, M. Enderle, T. Weber, B. Winn, M. Graves-Brook, J.M. Tranquada, T. Ziman, M. Fujita, G.E.W. Bauer, E. Saitoh, K. Kakurai, *Phys. Rev. Lett.* **125**, 027201 (2020).